






Processing of Bistatic SAR Data With Nonlinear Trajectory Using a Controlled-SVD Algorithm

Yi Xiong, *Member, IEEE*, Buge Liang , *Member, IEEE*, Hanwen Yu , *Senior Member, IEEE*, Jianlai Chen , *Member, IEEE*, Yanghao Jin , *Member, IEEE*, and Mengdao Xing , *Fellow, IEEE*

Abstract—The nonlinear trajectory and bistatic characteristics of general bistatic synthetic aperture radar (SAR) can cause severe two-dimensional space-variance in the echo signal, and therefore it is difficult to focus the echo signal directly using the traditional frequency-domain imaging algorithm based on the assumption of azimuth translational invariance. At present, the state-of-the-art nonlinear trajectory imaging algorithm is based on singular value decomposition (SVD), which has the problem that SVD may be not controlled, and thus may lead to a high imaging complexity or low imaging accuracy. Therefore, this article proposes a nonlinear trajectory SAR imaging algorithm based on controlled SVD (CSVD). First, the chirp scaling algorithm is used to correct the range space-variance, and then SVD is used to decompose the remaining azimuth space-variant phase, and the first two feature components after SVD are integrated to make them be represented by a new feature component. Finally, the new feature component is used for interpolation to correct the azimuth space-variance. The simulation results show that the proposed CSVD can further improve the image quality compared with SVD-Stolt.

Index Terms—Bastatic, nonlinear trajectory, singular value decomposition (SVD), synthetic aperture radar (SAR).

I. INTRODUCTION

COMPARED with monostatic SAR, bistatic synthetic aperture radar (SAR; BSAR) can observe the target from multiple angles and obtain more information because the transmitter and receiver are mounted on different platforms [1]. From the perspective of signal characteristics, BSAR can be divided into two configurations (i.e., translational-invariant BSAR (TI-BSAR) and translational-variant BSAR (TV-BSAR) [2]). The echo signal in TI-BSAR satisfies the

assumption of azimuth translational invariance. In this case, one only needs to consider the range space-variance of the echo signal, and the traditional frequency-domain imaging algorithm can achieve accurate imaging. However, TV-BSAR does not satisfy the aforementioned assumption. Therefore, the radar echo signal is both azimuth and range space-variant. For the two-dimensional space-variant echo signal, the traditional frequency-domain imaging algorithm based on the assumption of azimuth translational invariance is no longer valid.

TV-BSAR mainly includes four configurations: one-stationary BSAR [3], parallel nonequivalent velocity BSAR [4], nonparallel nonequivalent velocity BSAR, and general BSAR [5], [6]. Among them, the two-dimensional space-variance in general BSAR is most serious due to that the radar platform may not fly in strict accordance with the linear trajectory [7]. If the trajectory deviates from the straight line, the focusing quality will decrease, which makes focusing more difficult [8]. Therefore, the focusing of general BSAR is more difficult than the other three configurations. In addition, it should be noted that the nonlinear trajectory of monostatic SAR can also cause two-dimensional space-variance characteristics in radar echo signal [9]. In summary, there are two main types of frequency-domain imaging algorithms for the problem of two-dimensional space-variance.

- i) Scaling-based algorithms: This kind of algorithm corrects the space-variance characteristics of signal by the principle of scaling [10]–[14]. They can be used not only to correct the range space-variance, but also correct the azimuth space-variance of the signal. In particular, the chirp scaling algorithm (CSA) is generally used to correct the range space-variance [10], while the nonlinear CSA (NCSA) is usually used to correct the azimuth space-variance [12]. In addition, some scholars had successfully applied NCSA to the imaging of highly squinted SAR [11], [13]. It is worth mentioning that the image quality of scaling-based algorithms heavily depends on the order of the NCS function. In general, the higher the order of the NCS function, the higher the accuracy of the scaling, but its complexity will increase greatly. In order to consider the accuracy and complexity of the imaging algorithm at the same time, the order of the NCS function should not be too high. Therefore, scaling-based imaging algorithms could not meet the accuracy requirements in some complex situations.

Manuscript received February 1, 2021; revised April 24, 2021; accepted May 18, 2021. Date of publication May 28, 2021; date of current version June 14, 2021. This work was supported in part by the National Natural Science Foundation of China under Grant 61901531, and in part by the National Key Research and Development Program of China under Grant 2018YFC0810202-04. (*Corresponding author: Jianlai Chen.*)

Yi Xiong and Yanghao Jin are with the School of Automation, Central South University, Changsha 410083, China (e-mail: xy639692@163.com; jsanp0412@163.com).

Buge Liang and Jianlai Chen are with the School of Aeronautics and Astronautics, Central South University, Changsha 410083, China (e-mail: lbg21cen@163.com; jianlaichen@163.com).

Hanwen Yu is with the School of Resources and Environment, University of Electronic Science and Technology of China, Chengdu 611731, China (e-mail: yuhanwenxd@gmail.com).

Mengdao Xing is with the National Laboratory of Radar Signal Processing, Xidian University, Xi'an 710071, China (e-mail: xmd@xidian.edu.cn).

Digital Object Identifier 10.1109/JSTARS.2021.3084619

ii) Interpolation-based algorithms: The basic idea of this kind of algorithm is to find an accurate interpolation kernel to correct the space-variance of the signal [15]–[17]. For a SAR with linear trajectory, the typical Omega-k algorithm can be used to achieve the accurate imaging through interpolation. For TI-BSAR, after obtaining the accurate two-dimensional spectrum, Omega-k can still be used to achieve accurate imaging [16], [17]. However, the traditional Omega-k algorithm can only deal with the range space-variance of echo signal. For this issue, some scholars extend the interpolation-based algorithm from the range to the azimuth. In particular, an improved Omega-k algorithm is proposed in [2], which applies the interpolation to both the range and azimuth space-variance correction. This algorithm first linearizes the two-dimensional spectrum of the signal, and then derives a two-dimensional interpolation kernel for two-dimensional interpolation, but the process of solving the interpolation kernel is complicated and approximations are used, so the accuracy of the interpolation kernel may not be high enough. In order to further improve the accuracy of the interpolation kernel, singular value decomposition (SVD) is used to analyze the space-variance characteristics of the two-dimensional spectrum in [18], [19], and the accurate interpolation kernel can be obtained. The algorithm in [18], [19] corrects azimuth space-variance of the first two feature components by twice SVD-interpolation operations, so it is called the tandem SVD (TSVD) algorithm [18], [19]. Compared with the derivation of the interpolation kernel in [2], the method based on SVD is simpler and more accurate. Generally, the accuracy of interpolation-based imaging algorithms is higher than that of the scaling-based algorithm, but the large amount of calculation brought by interpolation also needs to be considered.

Although time-domain imaging algorithms, such as back projection (BP) algorithm, can be applied to general BSAR imaging with high accuracy, their efficiency is far lower than that of frequency-domain algorithms [20], [21]. Therefore, in order to consider the accuracy and efficiency of imaging, this article proposes a CSVD imaging algorithm for general BSAR, which belongs to an interpolation algorithm. The innovation of this article comes from [18], [19]. We further find that the SVD in [18], [19] is uncontrollable, and the first two feature components after SVD can be still integrated into a new feature component. Through the integration operation, the space-variant phase of the second feature component can be further reduced, and most of the space-variant phase of signal can be integrated into the new feature component. Based on the above processing, the CSVD algorithm proposed in this article can effectively avoid the uncontrollability of SVD.

This article is organized as follows. In Section II, the slant range model in the case of bistatic configuration and nonlinear trajectory is established, and the uncontrollability of SVD is analyzed. The proposed CSVD algorithm is detailed in Section III. In Section IV, simulation verification is performed. The conclusion is drawn in Section V.

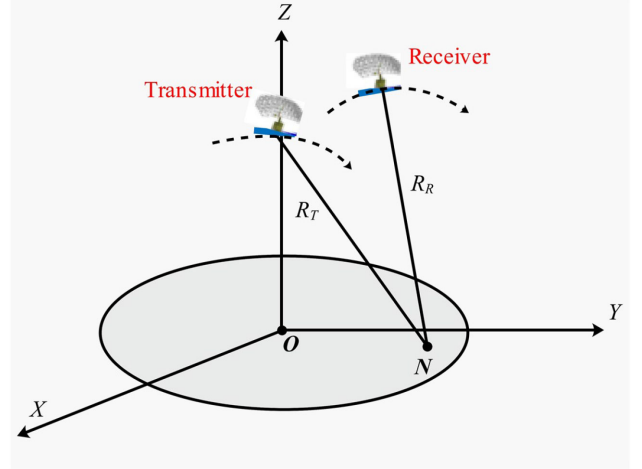


Fig. 1. Geometry of general BSAR.

II. MOTIVATION

A. Signal Modeling

The model of general BSAR is shown in Fig. 1. The motion trajectories of both transmitter and receiver flight platforms are nonlinear. Target O is located at scene center. The coordinate of an arbitrary target N on the scene is (x_n, y_n, z_n) , R_T and R_R , respectively, represent the instantaneous distance from target N to the transmitter and receiver, which can be expressed as follows:

$$R_T(t_a) = \sqrt{\begin{aligned} & \left(x_t + \left(v_{xt}t_a + \frac{1}{2}a_{xt}t_a^2 \right) - x_n \right)^2 \\ & + \left(y_t + \left(v_{yt}t_a + \frac{1}{2}a_{yt}t_a^2 \right) - y_n \right)^2 \\ & + \left(z_t + \left(v_{zt}t_a + \frac{1}{2}a_{zt}t_a^2 \right) - z_n \right)^2 \end{aligned}} \quad (1)$$

$$R_R(t_a) = \sqrt{\begin{aligned} & \left(x_r + \left(v_{xr}t_a + \frac{1}{2}a_{xr}t_a^2 \right) - x_n \right)^2 \\ & + \left(y_r + \left(v_{yr}t_a + \frac{1}{2}a_{yr}t_a^2 \right) - y_n \right)^2 \\ & + \left(z_r + \left(v_{zr}t_a + \frac{1}{2}a_{zr}t_a^2 \right) - z_n \right)^2 \end{aligned}} \quad (2)$$

where t_a denotes the azimuth time, and (x_t, y_t, z_t) and (x_r, y_r, z_r) denote the initial coordinate of the transmitter and receiver, respectively. (v_{xt}, v_{yt}, v_{zt}) and (v_{xr}, v_{yr}, v_{zr}) denote the initial speed of the transmitter and receiver, respectively. (a_{xt}, a_{yt}, a_{zt}) and (a_{xr}, a_{yr}, a_{zr}) denote the initial acceleration of the transmitter and receiver, respectively. The slant range of general BSAR can be expressed as

$$R(t_a) = R_R(t_a) + R_T(t_a). \quad (3)$$

TABLE I
MAIN SYSTEM PARAMETERS

Simulation parameter	Transmitter	Receiver
Initial position	(0, 0, 8000)	(0, 0, 8010)
Initial velocity	(0, 150, -2) m/sec	(0, 90, 2.1) m/sec
Acceleration	(0, 2.4, 3.6) m ² /sec	(0, 2.4, -1) m ² /sec
Carrier frequency	1.5GHz	
PRF	300Hz	
Signal bandwidth	100MHz	
Range sampling frequency	120MHz	

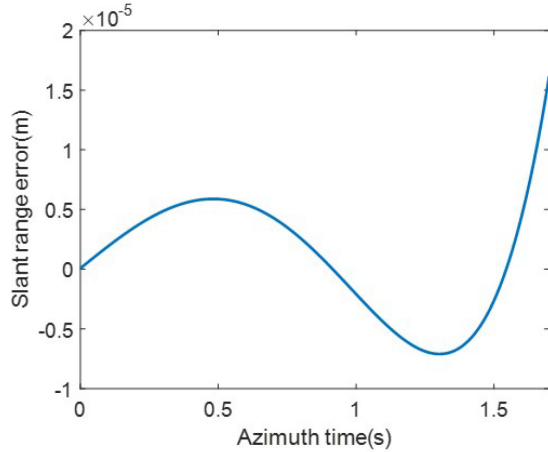


Fig. 2. Simulated slant range error of the fourth-order polynomial model.

Although (3) can accurately express the slant range model, the slant range is a double radical sign form due to the separation of the receiver and transmitter. In this case, it is difficult to directly use the principle of stationary phase to obtain the two-dimensional spectrum of the signal. Due to the advantages of high precision and analytical expression, the high-order polynomial slant range model is widely used in nonlinear trajectory SAR imaging [19]. This model expresses the slant range as a high-order polynomial of azimuth time. In order to balance the accuracy and complexity, we adopt the fourth-order polynomial model

$$R(t_a) \approx R_b + k_1 t_a + k_2 t_a^2 + k_3 t_a^3 + k_4 t_a^4 \quad (4)$$

where R_b denotes the range position of target N , k_i ($i = 1, 2, 3, 4$) is the i th-order polynomial coefficient, which are all related to the azimuth position and the range position of ground targets. With simulation parameters in Table I, the slant range error of the fourth-order polynomial model is simulated (see Fig. 2). It can be seen from Fig. 2 that the maximum error is less than $20 \mu\text{m}$. Therefore, the fourth-order polynomial model can accurately approximate the slant range of G-BSAR.

If the radar transmits a linear frequency modulated (LFM) signal, the echo signal in range-frequency and azimuth-time domain can be expressed as

$$S_1(f_r, t_a; R(t_a)) = W_r(f_r) A_a(t_a) \exp\left(-j\pi \frac{f_r^2}{\gamma}\right) \times \exp\left(-j \frac{2\pi}{c} (f_c + f_r) R(t_a)\right) \quad (5)$$

where f_r denotes the range frequency, $A_a(\cdot)$ and $W_r(\cdot)$ denote the azimuth envelope function and range envelope function, respectively. γ denotes the chirp rate of the LFM signal, f_c denotes the carrier frequency, and c denotes the light speed. For the slant range model in the form of a fourth-order polynomial, the two-dimensional spectrum can be obtained easily by using the method of series reversion [22], which is as follows:

$$\begin{aligned} \phi(f_r, f_a; X, R_b) &= -\pi \frac{f_r^2}{\gamma} - 2\pi \left(\frac{f_0 + f_r}{c}\right) R_b \\ &+ 2\pi \frac{c}{4k_2(f_0 + f_r)} \left(f_a + (f_0 + f_r) \frac{k_1}{c}\right)^2 \\ &+ 2\pi \frac{c^2 k_3}{8k_2^3(f_0 + f_r)^2} \left(f_a + (f_0 + f_r) \frac{k_1}{c}\right)^3 \\ &+ 2\pi \frac{c^3(9k_3^2 - 4k_2 k_4)}{64k_2^5(f_0 + f_r)^3} \left(f_a + (f_0 + f_r) \frac{k_1}{c}\right)^4 \end{aligned} \quad (6)$$

where $\phi(f_r, f_a; X, R_b)$ denotes the phase of the two-dimensional spectrum, f_a denotes the azimuth frequency, and X denotes the azimuth position of target N .

B. Uncontrollability Analysis of SVD

In order to illustrate the uncontrollability of SVD, we do not consider the range space-variance first. Therefore, the two-dimensional spectrum of the signal can be simplified as $\phi(f_a, X)$. After SVD, the two-dimensional spectrum of the signal can be expressed as the sum of multiple feature components

$$\phi(f_a, X) = \sum_{i=1}^n u_i(X)_{n \times 1} \cdot S(i, i) \cdot v_i(f_a)_{1 \times n} \quad (7)$$

where $u_i(X)S(i, i)v_i(f_a)$ denotes the i th feature component, and each feature component can be decomposed into the product of the function of the azimuth position and the azimuth frequency. Normally, the first feature component in (7) is the largest, and the subsequent feature components decrease in turn. Generally, the signal after SVD has the following two cases.

- i) Case #1: The two-dimensional spectrum of the signal can be completely represented by only one feature component.
- ii) Case #2: The two-dimensional spectrum of the signal must be represented by two feature components.

In Case #1, all the azimuth space-variant phase of the two-dimensional spectrum is included in the first feature component. At this time, the first feature component can be used for interpolation to complete the focusing of all azimuth targets. However, in Case #2, the phase of two-dimensional spectrum after SVD

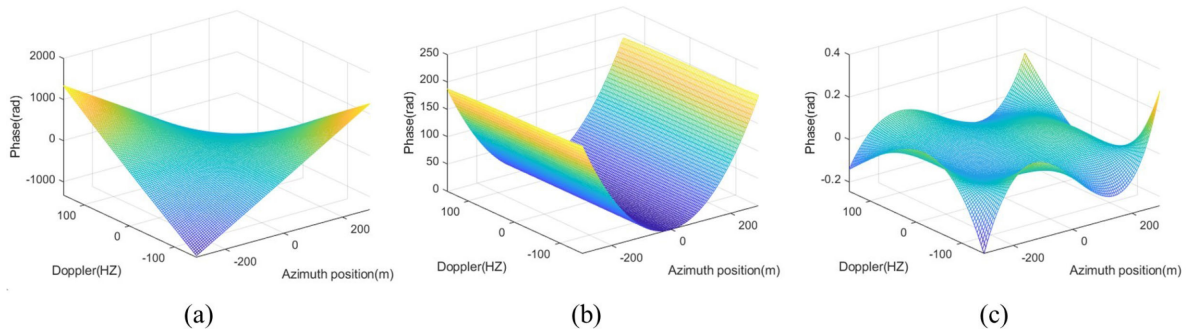


Fig. 3. Feature components of the two-dimensional spectrum after SVD without integration. Phases of (a) the first feature component, (b) the second feature component, and (c) the sum of remaining of feature components.

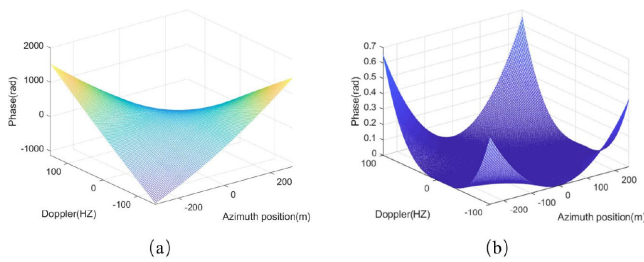


Fig. 4. Results after integration. Phases of (a) the new feature component, and (b) the residual azimuth space-variance.

can be approximately expressed as

$$\phi(f_a, X) = u_1(X)S(1, 1)v_1(f_a) + u_2(X)S(2, 2)v_2(f_a). \quad (8)$$

For the signal in (8), it is difficult to ensure that all the azimuth space-variant phase is within the first feature component. When the azimuth space-variant phase of the second feature component after SVD is large, it will cause defocusing if only the first feature component is used for interpolation.

From the above analysis of the two cases of SVD results, it can be seen that the uncontrollability of SVD is expressed as that whether the signal can be represented by one feature component is uncontrollable after SVD. Through further research on the results of SVD, we found that the azimuth space-variant terms of the first feature component and the second feature component can be further integrated (see Section III for the detailed integration process) in Case #2, and thus the two-dimensional spectrum of the signal can be expressed as the sum of a new feature component and a residual phase. Moreover, the residual phase can be regraded as space-invariant. Based on this conclusion, we can add integration operations to make the entire decomposition process controllable, that is, the decomposition result can always be fully represented by one feature component.

According to the parameters in Table I, Figs. 3 and 4, respectively, show the results of SVD without intergration and the results of adding integration operations. It can be seen from Fig. 3 that the values of the first feature component and the second feature component are much greater than $\pi/4$ rads. The sum of the remaining feature components is smaller than $\pi/4$ rads and

can be ignored. Therefore, the signal needs to be represented by two feature components, and additional processing is required to complete focusing, such as the second interpolation in [19], which will greatly reduce the imaging efficiency. However, it can be seen from Fig. 4 that the signal can be expressed in the form of the sum of a new feature component in Fig. 4(a) and a residual azimuth space-variant phase in Fig. 4(b) by integration operations. The values of the residual azimuth space-variant phase is less than 0.7 rads and can be ignored. Therefore, the signal can be completely represented by the new feature component. Through the operation of integration, we can directly use one Stolt-interpolation to complete the focusing without additional processing steps.

III. ALGORITHM

Based on the signal model and the uncontrollability analysis of SVD in Section II, this article develops a CSVD algorithm for general BSAR. The flowchart of the algorithm is shown in Fig. 5. The algorithm mainly includes two steps: firstly, the CSA is used to correct the range space-variance, and then the controlled SVD is used to correct the azimuth space-variance.

A. RCMC by Using CSA

For the range space-variance of the signal, the traditional frequency-domain algorithm can be used for accurate correction. Here we use CSA to complete range cell migration correction (RCMC). The scaling function, RCMC function, and range-matched filter function in CS algorithm can be constructed as in [10]. After the RCMC, the signals in azimuth time-domain can be expressed as

$$S_S(t_a, X) = \exp\left(-\frac{2\pi}{\lambda}R(t_a, X)\right). \quad (9)$$

B. Correction of Azimuth-Variance by Using CSVD

After the RCMC, the phase of the signal can be expressed by (8). Both the azimuth position function and the azimuth frequency function in (8) can be expressed by Taylor series as

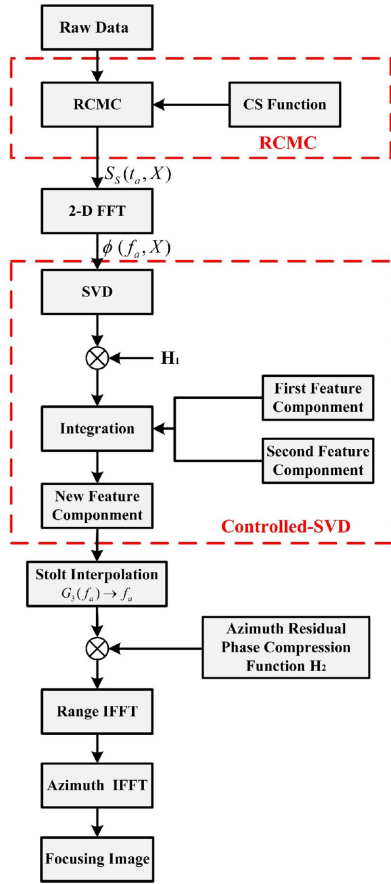


Fig. 5. Flowchart of the proposed CSVD algorithm.

$$\begin{aligned}
 u_1(X) &\approx u_1(X)|_{X=0} + \left. \frac{\partial u_1(X)}{\partial X} \right|_{X=0} \\
 &\quad \cdot X + \left. \frac{1}{2} \frac{\partial^2 u_1(X)}{\partial X^2} \right|_{X=0} \cdot X^2 \\
 &= a_0 + a_1 X + a_2 X^2 \\
 u_2(X) &\approx u_2(X)|_{X=0} + \left. \frac{\partial u_2(X)}{\partial X} \right|_{X=0} \\
 &\quad \cdot X + \left. \frac{1}{2} \frac{\partial^2 u_2(X)}{\partial X^2} \right|_{X=0} \cdot X^2 \\
 &= b_0 + b_1 X + b_2 X^2 \\
 v_1(f_a) &\approx v_1(f_a)|_{f_a=0} + \left. \frac{\partial v_1(f_a)}{\partial f_a} \right|_{f_a=0} \\
 &\quad \cdot f_a + \left. \frac{1}{2} \frac{\partial^2 v_1(f_a)}{\partial f_a^2} \right|_{f_a=0} \cdot f_a^2 \\
 &\quad + \left. \frac{1}{3!} \frac{\partial^3 v_1(f_a)}{\partial f_a^3} \right|_{f_a=0}
 \end{aligned} \tag{10}$$

$$\begin{aligned}
 &\cdot f_a^3 + \left. \frac{1}{4!} \frac{\partial^4 v_1(f_a)}{\partial f_a^4} \right|_{f_a=0} \cdot f_a^4 \\
 &= c_0 + c_1 f_a + c_2 f_a^2 + c_3 f_a^3 + c_4 f_a^4
 \end{aligned} \tag{12}$$

$$\begin{aligned}
 v_2(f_a) &\approx v_2(f_a)|_{f_a=0} + \left. \frac{\partial v_2(f_a)}{\partial f_a} \right|_{f_a=0} \\
 &\quad \cdot f_a + \left. \frac{1}{2} \frac{\partial^2 v_2(f_a)}{\partial f_a^2} \right|_{f_a=0} \cdot f_a^2 \\
 &\quad + \left. \frac{1}{3!} \frac{\partial^3 v_2(f_a)}{\partial f_a^3} \right|_{f_a=0} \cdot f_a^3 + \left. \frac{1}{4!} \frac{\partial^4 v_2(f_a)}{\partial f_a^4} \right|_{f_a=0} \cdot f_a^4 \\
 &= d_0 + d_1 f_a + d_2 f_a^2 + d_3 f_a^3 + d_4 f_a^4.
 \end{aligned} \tag{13}$$

Submitting (10)–(13) to (8), the phase of the signal can be expressed as

$$\begin{aligned}
 \phi'(f_a, X) &\approx (A_0 + A_1 X + A_2 X^2) f_a + (B_0 + B_1 X + B_2 X^2) f_a^2 \\
 &\quad + (C_0 + C_1 X + C_2 X^2) f_a^3 + (D_0 + D_1 X + D_2 X^2) f_a^4
 \end{aligned} \tag{14}$$

where

$$\left\{ \begin{array}{l}
 A_0 = a_0 c_1 + b_0 d_1 \\
 A_1 = a_1 c_1 + b_1 d_1 \\
 A_2 = a_2 c_1 + b_2 d_1 \\
 B_0 = a_0 c_2 + b_0 d_2 \\
 B_1 = a_1 c_2 + b_1 d_2 \\
 B_2 = a_2 c_2 + b_2 d_2 \\
 C_0 = a_0 c_3 + b_0 d_3 \\
 C_1 = a_1 c_3 + b_1 d_3 \\
 C_2 = a_2 c_3 + b_2 d_3 \\
 D_0 = a_0 c_4 + b_0 d_4 \\
 D_1 = a_1 c_4 + b_1 d_4 \\
 D_2 = a_2 c_4 + b_2 d_4.
 \end{array} \right. \tag{15}$$

It should be noted that the constant term in (14) is ignored because it has no effect on focusing. In addition, the phase terms that are not related to the azimuth position in (14) can be compensated by using

$$H_1 = \exp(-A_0 f_a - B_0 f_a^2 - C_0 f_a^3 - D_0 f_a^4). \tag{16}$$

(11) After the compensation, the phase of azimuth signal in (14) becomes

$$\begin{aligned}
 \phi'(f_a, X) &\approx (A_1 X + A_2 X^2) f_a + (B_1 X + B_2 X^2) f_a^2 \\
 &\quad + (C_1 X + C_2 X^2) f_a^3 + (D_1 X + D_2 X^2) f_a^4.
 \end{aligned} \tag{17}$$

Next, we integrate (17). The whole integration operation includes three steps, namely, integrating quadratic phase term, integrating cubic phase term, and integrating quartic phase term.

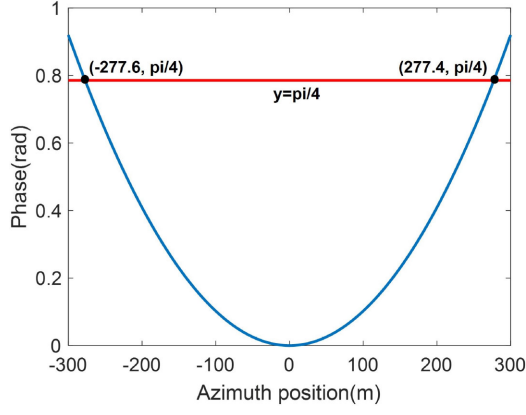


Fig. 6. Absolute value of the residual azimuth space-variant phase varying with the azimuth position of target.

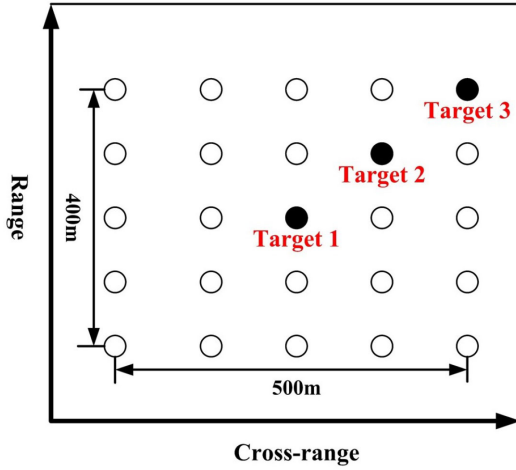


Fig. 7. Scene of 400 m (range) \times 500 m (azimuth); 25 targets are evenly distributed in the scene.

TABLE II
IMAGING EVALUATION RESULTS OF SELECTED TARGETS

Algorithm	Target	Azimuth PSLR(dB)	Azimuth ISLR(dB)
Omega-k in [2]	Target2	-12.92	-9.56
	Target3	-12.00	-8.96
SVD-Stolt in [23]	Target2	-13.18	-9.91
	Target3	-12.44	-9.74
CSVD	Target2	-13.20	-10.08
	Target3	-13.15	-10.10

1) *Integration of Quadratic Phase Term:* At this stage, the cubic and quartic phase terms are not considered. First, the linear and quadratic phase terms are integrated to a new feature component. The integration process is shown in (18).

$$\begin{aligned}\phi_1(f_a, X) &= (A_1X + A_2X^2)f_a + (B_1X + B_2X^2)f_a^2 \\ &= (A_1X + A_2X^2)f_a + \left(B_1X + \frac{A_2B_1}{A_1}X^2\right)f_a^2 \\ &\quad - \frac{A_2B_1}{A_1}X^2f_a^2 + B_2X^2f_a^2\end{aligned}$$

$$\begin{aligned}&= \underbrace{(B_1X + B_2X^2)(q_1f_a + f_a^2)}_{F_1(X)G_1(f_a)} \\ &\quad + \underbrace{(B_2 - B_2')X^2f_a^2}_{\varphi_1(X, f_a)}\end{aligned}\quad (18)$$

where $q_1 = A_1/B_1$ and $B_2' = A_2B_1/A_1$. $F_1(X)G_1(f_a)$ is the new feature component after integrating the quadratic phase term, and $\varphi_1(X, f_a)$ is the residual azimuth space-variant phase after integrating the quadratic phase term.

2) *Integration of Cubic Phase Term:* The second step is to integrate (18) and the cubic phase term. The integration process is shown in (19).

$$\begin{aligned}\phi_2(f_a, X) &= (B_1X + B_2X^2)(q_1f_a + f_a^2) \\ &\quad + (C_1X + C_2X^2)f_a^3 + \varphi_1(X, f_a) \\ &= \underbrace{(C_1X + C_2X^2)[q_2(q_1f_a + f_a^2) + f_a^3]}_{F_2(X)G_2(f_a)} \\ &\quad + \underbrace{\varphi_1(X, f_a) + (C_2 - C_2')X^2f_a^3}_{\varphi_2(X, f_a)}\end{aligned}\quad (19)$$

where $q_2 = B_1/C_1$ and $C_2' = B_2'C_1/B_1$. $F_2(X)G_2(f_a)$ is the new feature component after integrating the cubic phase term, and $\varphi_2(X, f_a)$ is the residual azimuth space-variant phase after integrating the cubic phase term.

3) *Integration of Quartic Phase Term:* The third step is to integrate (19) and the quartic phase term. The specific integration process is shown in (20).

$$\begin{aligned}\phi_3(X, f_a) &= (C_1X + C_2X^2)[q_2(q_1f_a + f_a^2) + f_a^3] \\ &\quad + (D_1X + D_2X^2)f_a^4 + \varphi_2(X, f_a) \\ &= \underbrace{(D_1X + D_2X^2)\{q_3[q_2(q_1f_a + f_a^2) + f_a^3] + f_a^4\}}_{F_3(X)G_3(f_a)} \\ &\quad + \underbrace{\varphi_2(X, f_a) + (D_2 - D_2')X^2f_a^4}_{\varphi_3(X, f_a)}\end{aligned}\quad (20)$$

where $q_3 = C_1/D_1$ and $D_2' = C_2'D_1/C_1$. $F_3(X)G_3(f_a)$ is the new feature component after integrating the quartic phase term, and $\varphi_3(X, f_a)$ is the residual azimuth space-variant phase after integrating the quartic phase term.

After the integration, the phase in (17) can be expressed as

$$\phi'(X, f_a) = F_3(X)G_3(f_a) + \varphi_3(X, f_a).\quad (21)$$

It can be seen from (21) that most of the azimuth space-variant phase after the integration is included in only one feature component [i.e., $F_3(X)G_3(f_a)$]. The absolute value of the residual azimuth space-variant phase is less than $\pi/4$ rads (see Fig. 4). Therefore, it can be approximately compensated by using

$$H_2 = \exp(-\varphi_3(X_0, f_a))\quad (22)$$

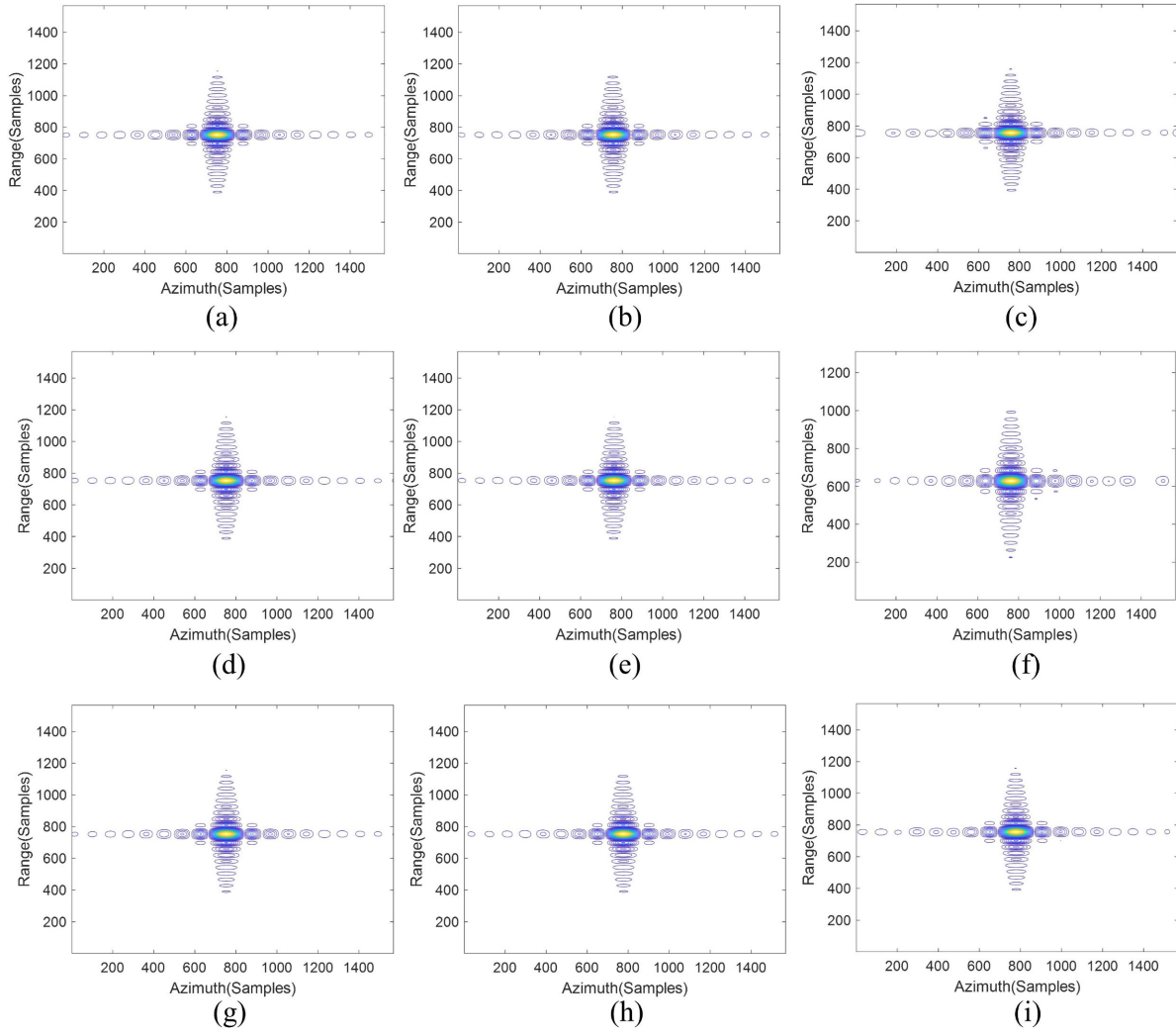


Fig. 8. Contours of the selected targets by using (a)–(c) improved Omega-k algorithm in [2], (d)–(f) SVD-Stolt algorithm in [23], and (g)–(i) the proposed algorithm. The first to third columns correspond to target 1, target 2, and target 3, respectively.

where X_0 denotes the azimuth position of the target at scene center. After the compensation, the phase of azimuth signal in (21) can be expressed as

$$\phi'(X, f_a) = F_3(X)G_3(f_a). \quad (23)$$

For the phase in (23), one can easily perform the interpolation operation to correct azimuth space-variance. The interpolation kernel is $G_3(f_a) \rightarrow f_a$. After the interpolation operation, the phase of azimuth signal is given by

$$\phi'(X, f_a) = F_3(X) \cdot f_a. \quad (24)$$

For the signal of (24), we can directly use the azimuth IFFT to complete the focus imaging.

C. Analysis of Applicable Condition

When the platform has acceleration, especially when the acceleration value is relatively large, the azimuth space-variance becomes more serious, which may cause the control ability of the proposed algorithm for SVD decrease. Therefore, the proposed

algorithm is proposed under the condition that the acceleration changes little and its value is relatively small. In addition, the CSVD algorithm proposed in this article has a prerequisite: the absolute value of the residual azimuth space-variant phase during the entire imaging process must be less than $\pi/4$ rads, namely,

$$\max \left\{ \underbrace{\left| \varphi_{r1}(X, f_a) + \varphi_{r2}(X, f_a) + \varphi_{r3}(X, f_a) \right|}_{\varphi_r} \right\} < \frac{\pi}{4}. \quad (25)$$

As shown in (25), the residual azimuth space-variant phase of the proposed algorithm consists of three parts, in which $\varphi_{r1}(X, f_a)$ denotes the residual azimuth space-variance phase after integration, $\varphi_{r2}(X, f_a)$ denotes the sum of the remaining feature components after SVD except the first two feature components, and $\varphi_{r3}(X, f_a)$ denotes the phase difference between (8) and (14).

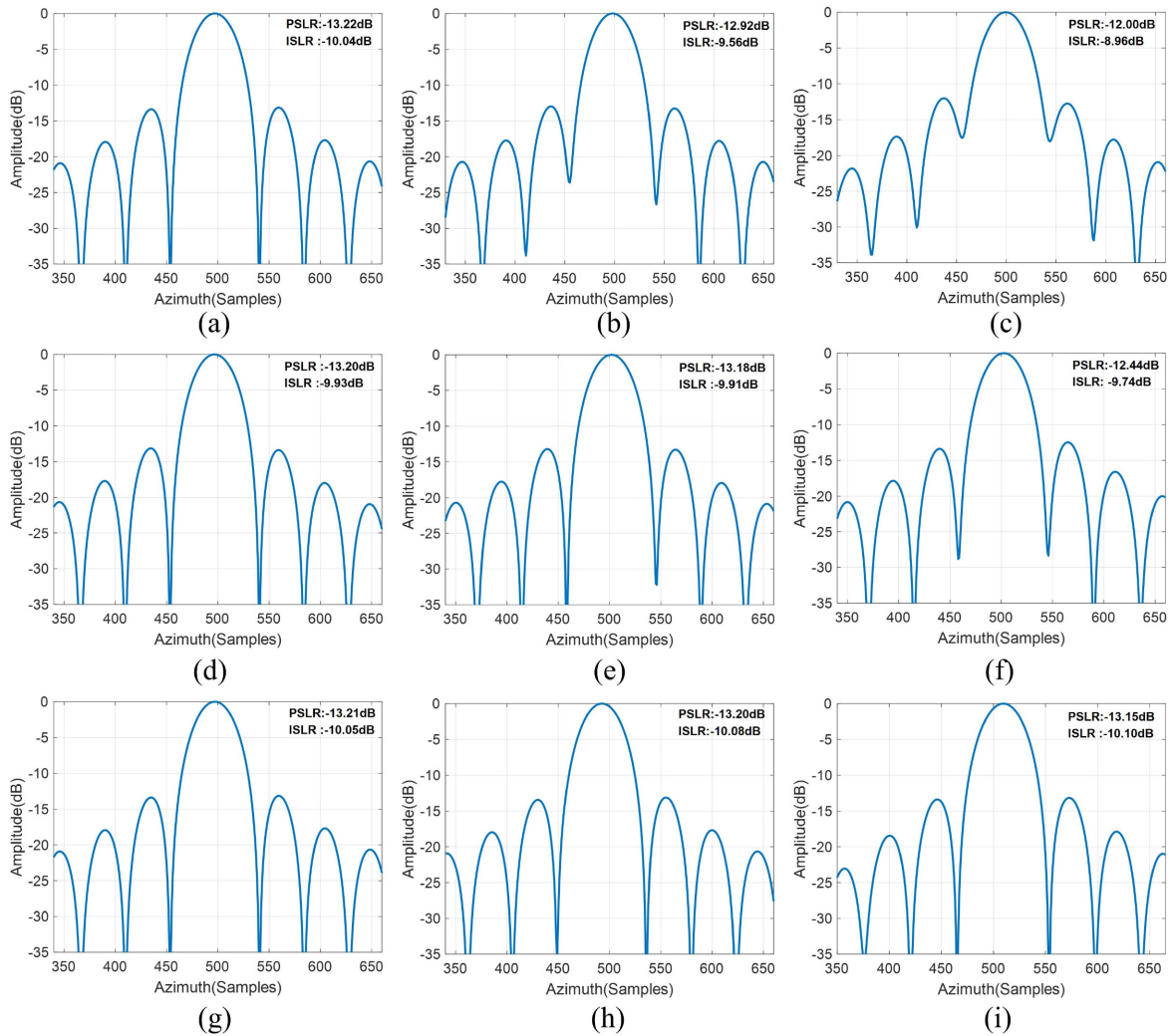


Fig. 9. Azimuth profiles of the selected targets by using (a)–(c) improved Omega-k algorithm in [2], (d)–(f) SVD-Stolt algorithm in [23], and (g)–(i) the proposed algorithm. The first to third columns correspond to target 1, target 2, and target 3, respectively.

According to the parameters in Table I, Fig. 6 shows the absolute value of the residual azimuth space-variant phase varying with the azimuth position. The larger the scene width, the larger the residual azimuth space-variant phase. Subject to the constraints of (25), it can be seen from Fig. 6 that the scene size of the proposed algorithm should be smaller than about 550 m.

IV. VERIFICATION BY SIMULATED RESULT

In this section, we will verify the accuracy of the proposed imaging algorithm by simulation results. In addition, we use the improved Omega-k algorithm in [2] and SVD-Stolt algorithm in [23] as references to verify the superiority of the proposed algorithm.

The simulation parameters are shown in Tables I. A set of 5×5 targets (range \times azimuth) (see Fig. 7) are placed on the ground uniformly with a scene size of $400 \times 500 \text{ m}^2$ (range \times azimuth). Target 1 is at the scene center, target 3 is at the

scene edge, and target 2 is located between target 1 and target 3. In order to verify the effectiveness and superiority of the proposed algorithm, we use the proposed algorithm and the reference algorithms to evaluate targets (1–3). Their contours and azimuth profiles are shown in Figs. 8 and 9, respectively. In addition, the quantitative evaluation results are shown in Table II, including the azimuth PSLR and the azimuth ISLR of these targets.

It can be seen from Fig. 8 that the proposed algorithm can focus all targets well after integrating the feature components, while defocusing still exist at the edge points for the reference algorithms. In addition, as shown in Fig. 9 and Table II, the focusing quality of the reference algorithms is lower than that of the proposed algorithm. Moreover, both the proposed algorithm and the reference algorithms only use one interpolation operation in the imaging process, and the computational complexity of the three algorithms is the same. Therefore, the proposed algorithm can further improve the imaging quality without increasing the amount of calculation.

V. CONCLUSION

This article proposes a CSVD algorithm to solve the uncontrollable problem of the existing SVD-based algorithm for nonlinear trajectory imaging. First, the CSA is used to correct range space-variance, and then we perform SVD on the azimuth space-variance phase. In order to avoid the uncontrollability of SVD, we introduce an integration operation to represent the phase of the signal as only one feature component. Finally, we use Stolt-interpolation to correct the azimuth space-variance. Simulation results show that compared with the SVD-Stolt algorithm, the proposed algorithm can effectively control the results of SVD, which can further improve the imaging quality.

REFERENCES

- [1] A. Moreira, P. Prats-Iraola, M. Younis, G. Krieger, I. Hajnsek, and K. P. Papathanassiou, "A tutorial on synthetic aperture radar," *IEEE Geosci. Remote Sens. Mag.*, vol. 1, no. 1, pp. 6–43, Mar. 2013.
- [2] J. Wu, Z. Li, Y. Huang, J. Yang, and Q. H. Liu, "A generalized Omega-K algorithm to process translationally variant Bistatic-SAR data based on two-dimensional Stolt mapping," *IEEE Trans. Geosci. Remote Sens.*, vol. 52, no. 10, pp. 6597–6614, Oct. 2014.
- [3] Z. Li, J. Wu, W. Li, Y. Huang, and J. Yang, "One-stationary bistatic side-looking SAR imaging algorithm based on extended keystone transforms and nonlinear chirp scaling," *IEEE Geosci. Remote Sens. Lett.*, vol. 10, no. 2, pp. 211–215, Mar. 2013.
- [4] Y. Yonghong and P. Yiming, "Azimuth space-variant properties of BiSAR with nonequal velocities," *J. Syst. Eng. Electron.*, vol. 19, no. 5, pp. 919–922, 2008.
- [5] G. G. Liu, L. R. Zhang, and X. Liu, "General Bistatic SAR data processing based on extended nonlinear chirp scaling," *IEEE Geosci. Remote Sens. Lett.*, vol. 10, no. 5, pp. 976–980, Sep. 2013.
- [6] K. Yang, F. He, and D. Liang, "A two-dimensional spectrum for general Bistatic SAR processing," *IEEE Geosci. Remote Sens. Lett.*, vol. 7, no. 1, pp. 108–112, Jan. 2010.
- [7] J. Chen, M. Xing, X. Xia, J. Zhang, B. Liang, and D. Yang, "SVD-based ambiguity function analysis for nonlinear trajectory SAR," *IEEE Trans. Geosci. Remote Sens.*, vol. 59, no. 4, pp. 3072–3087, Apr. 2021.
- [8] D. R. Kirk, R. P. Maloney, and M. E. Davis, "Impact of platform motion on wide angle synthetic aperture radar (SAR) image quality," *Proc. IEEE Radar Conf. Radar Next Millennium*, 1999, pp. 41–46.
- [9] T. Zhang, Z. Ding, W. Tian, T. Zeng, and W. Yin, "A 2-D nonlinear chirp scaling algorithm for high squint GEO SAR imaging based on optimal azimuth polynomial compensation," *IEEE J. Sel. Topics Appl. Earth Observ. Remote Sens.*, vol. 10, no. 12, pp. 5724–5735, Dec. 2017.
- [10] R. K. Raney, H. Runge, R. Bamler, I. G. Cumming, and F. H. Wong, "Precision SAR processing using chirp scaling," *IEEE Trans. Geosci. Remote Sens.*, vol. 32, no. 4, pp. 786–799, Jul. 1994.
- [11] Z. Li *et al.*, "A frequency-domain imaging algorithm for highly squinted SAR mounted on maneuvering platforms with nonlinear trajectory," *IEEE Trans. Geosci. Remote Sens.*, vol. 54, no. 7, pp. 4023–4038, Jul. 2016.
- [12] H. An, J. Wu, Z. Sun, and J. Yang, "A two-step nonlinear chirp scaling method for multichannel GEO Spaceborne-Airborne Bistatic SAR spectrum reconstructing and focusing," *IEEE Trans. Geosci. Remote Sens.*, vol. 57, no. 6, pp. 3713–3728, Jun. 2019.
- [13] D. Li, G. Liao, W. Wang, and Q. Xu, "Extended azimuth nonlinear chirp scaling algorithm for Bistatic SAR processing in high-resolution highly squinted mode," *IEEE Geosci. Remote Sens. Lett.*, vol. 11, no. 6, pp. 1134–1138, Jun. 2014.
- [14] J. Chen, J. Zhang, Y. Jin, H. Yu, B. Liang, and D.-G. Yang, "Real-time processing of Spaceborne SAR data with nonlinear trajectory based on variable PRF," *IEEE Trans. Geosci. Remote Sens.*, to be published, doi: [10.1109/TGRS.2021.3067945](https://doi.org/10.1109/TGRS.2021.3067945).
- [15] C. Cafforio, C. Prati, and F. Rocca, "SAR data focusing using seismic migration techniques," *IEEE Trans. Aerosp. Electron. Syst.*, vol. 27, no. 2, pp. 194–207, Mar. 1991.
- [16] B. Liu, T. Wang, Q. Wu, and Z. Bao, "Bistatic SAR data focusing using an Omega-k algorithm based on method of series reversion," *IEEE Trans. Geosci. Remote Sens.*, vol. 47, no. 8, pp. 2899–2912, Aug. 2009.
- [17] X. Qiu, D. Hu, and C. Ding, "An Omega-K algorithm with phase error compensation for Bistatic SAR of a translational invariant case," *IEEE Trans. Geosci. Remote Sens.*, vol. 46, no. 8, pp. 2224–2232, Aug. 2008.
- [18] J. Chen *et al.*, "A TSVD-NCS algorithm in range-doppler domain for geosynchronous synthetic aperture radar," *IEEE Geosci. Remote Sens. Lett.*, vol. 13, no. 11, pp. 1631–1635, Nov. 2016.
- [19] J. Chen, G. Sun, M. Xing, B. Liang, and Y. Gao, "Focusing improvement of curved trajectory Spaceborne SAR based on optimal LRWC preprocessing and 2-D singular value decomposition," *IEEE Trans. Geosci. Remote Sens.*, vol. 57, no. 7, pp. 4246–4258, Jul. 2019.
- [20] L. M. H. Ulander, H. Hellsten, and G. Stenstrom, "Synthetic-aperture radar processing using fast factorized back-projection," *IEEE Trans. Aerosp. Electron. Syst.*, vol. 39, no. 3, pp. 760–776, Jul. 2003.
- [21] M. Rodriguez-Cassola, P. Prats, G. Krieger, and A. Moreira, "Efficient time-domain image formation with precise topography accommodation for general Bistatic SAR configurations," *IEEE Trans. Aerosp. Electron. Syst.*, vol. 47, no. 4, pp. 2949–2966, Oct. 2011.
- [22] Y. L. Neo, F. Wong, and I. G. Cumming, "A two-dimensional spectrum for Bistatic SAR processing using series reversion," *IEEE Geosci. Remote Sens. Lett.*, vol. 4, no. 1, pp. 93–96, Jan. 2007.
- [23] D. D'Aria and A. Monti Guarnieri, "High-resolution spaceborne SAR focusing by SVD-Stolt," *IEEE Geosci. Remote Sens. Lett.*, vol. 4, no. 4, pp. 639–643, Oct. 2007.



Yi Xiong (Member, IEEE) was born in Changde, Hunan, China, in 1998. He is currently working toward the Ph.D. degree with Central South University (CSU), Changsha, China.

His research interests include bistatic SAR imaging and nonlinear trajectory SAR imaging.



Buge Liang (Member, IEEE) received the B.S. and Ph.D. degrees from the National University of Defense Technology (NUDT), Changsha, China, in 2001 and 2007, respectively.

He is a Full Professor with Central South University (CSU), Changsha. His research interests include electromagnetic measurement technologies, high-power nanosecond pulsers, and ultrawideband (UWB) radar.



Hanwen Yu (Senior Member, IEEE) was born in Xi'an, Shaanxi, China, in 1985. He received the B.S. and Ph.D. degrees in electronic engineering from the Xidian University, Xi'an, China, in 2007 and 2012, respectively.

He was a Postdoctoral Research Fellow with the Department of Civil and Environmental Engineering, National Center for Airborne Laser Mapping, University of Houston, Houston, TX, USA. He is currently a Full Professor with the School of Resources and Environment, University of Electronic Science and Technology of China, Chengdu, China. He has authored or coauthored more than 35 research articles in high-impact peer-reviewed journals, such as the IEEE TRANSACTIONS ON GEOSCIENCE AND REMOTE SENSING and the IEEE TRANSACTIONS ON IMAGE PROCESSING, AND REMOTE SENSING OF ENVIRONMENT. His research interests include phase unwrapping, machine learning, and synthetic aperture radar (SAR) interferometry (InSAR) signal processing and applications.

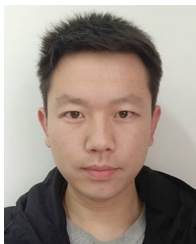
Dr. Yu has reviewed more than 200 manuscripts for more than 20 different journals. He has received the Recognition of Best Reviewer of the IEEE TRANSACTIONS ON GEOSCIENCE AND REMOTE SENSING in 2019. He serves as a Topical Associate Editor of the IEEE TRANSACTIONS ON GEOSCIENCE AND REMOTE SENSING, and an Associate Editor of the *IEEE Geoscience and Remote Sensing Magazine*. He has guest edited five special issues on InSAR remote sensing for different journals (e.g., *IEEE Journal of Selected Topics in Applied Earth Observations and Remote Sensing* and *MDPI Sensors*).



Jianlai Chen (Member, IEEE) was born in Hengyang, Hunan, China, in 1990. He received the B.S. degree in electronic engineering and the Ph.D. degree in signal and information processing from Xidian University, Xi'an, China, in 2013 and 2018, respectively.

He is currently an Associate Professor with Central South University (CSU), Changsha, China. He has authored or coauthored one book and more than 20 research articles in high-impact peer-reviewed journals. His research interests include synthetic aperture radar (SAR) imaging, SAR motion compensation (MoCo) and autofocus, and machine learning.

Dr. Chen serves as the Guest Editor for the Special Issues of the *Remote Sensing* and *MDPI Sensors*.



Yanghao Jin (Member, IEEE) received the B.S. degree from Xidian University, Xi'an, China, in 2016. He is currently working toward the Ph.D. degree with Central South University (CSU), Changsha, China.

His research interests include high-resolution SAR imaging and nonlinear trajectory SAR imaging.



Mengdao Xing (Fellow, IEEE) received the B.S. and Ph.D. degrees from Xidian University, Xi'an, Shaanxi, China, in 1997 and 2002, respectively.

He is currently a Professor with the National Laboratory of Radar Signal Processing, Xidian University. He is the Dean with the Academy of Advanced Interdisciplinary Research Department, Xidian University. His research interests include synthetic aperture radar (SAR), SAR interferometry (InSAR), inversed synthetic aperture radar (ISAR), sparse signal processing, and microwave remote sensing. He has

authored or co-authored more than 200 refereed scientific journal papers, and two books about SAR signal processing. The total citation times of his research are greater than 10 000 (H-index 50). He was rated as Most Cited Chinese Researchers by Elsevier. He has achieved over 50 authorized China patents.

Dr. Xing was Editor of several special issues on *IEEE Geoscience and Remote Sensing Magazine* and *IEEE Journal of Selected Topics in Applied Earth Observations and Remote Sensing*. Currently, he serves as the Associate Editor for radar remote sensing of the *IEEE TRANSACTIONS ON GEOSCIENCE AND REMOTE SENSING* and the Editor-in-Chief of *MDPI Sensors*.